A Versatile Preparation of Mesoporous Single Layered Transition Metal Sulfide/Carbon Composites for Enhanced Sodium Storage

Xing Zhang [1], Wei Weng [2], Hao Gu [3], Zibo Hong [1], Wei Xiao [2], Feng (Ryan) Wang [3], Wei Li [4], Dong Gu [1,*]

[1] The Institute for Advanced Studies, Wuhan University, Wuhan, Hubei 430072, P. R. China

[2] College of Chemistry and Molecular Sciences, Wuhan University, Wuhan, Hubei 430072, P. R. China

[3] Department of Chemical Engineering, University College London, Roberts Building, Torrington Place, London WC1E 7JE, UK

[4] Department of Chemistry, Fudan University, Shanghai 200433, P. R. China

*Corresponding author:

E-mail address: DGu@whu.edu.cn

Abstract

Transition metal sulfides are promise electrochemical energy storage materials due to their abundant active sites, large inter-layer space and high theoretical capacities. Especially for sodium storage. However, the low conductivity and poor cycling stability at high current densities hampered their applications. Herein, we report a versatile dual-templates method to elaborate ordered mesoporous single layered MoS_2/carbon composite with high specific area, uniform pore size and large pore volume. The single layered MoS_2 is confined in the carbon matrix. The mesopores between the composite nanorods provide fast electrolyte diffusion. The obtained nanocomposite shows a high sodium storage capability, excellent rate capacity, and very good cycling performance. A 310 mAh g^{-1} capacity can remains at 5.0 A g^{-1} after 2500 cycles. Furthermore, a SIB full cell composed the MoS_2/carbon composite anode and a $Na_3V_2(PO_4)_3$ (NVP) cathode maintains a specific capacity of 330 mA h g^{-1} at 1.0 A g^{-1} during 100 cycles. The mechanism is investigated by *in situ* and *ex situ* characterizations as well as density functional theory (DFT) calculations.

2

WILEY-VCH

1. Introduction

Sodium ion batteries (SIBs) has been considered as auspicious alternatives for the state-of-the-art lithium ion batteries (LIBs) because of the rich natural abundance (Na: 2.3 wt% *vs.* Li: 0.0017 wt%). [1-6] However, owing to the bigger ionic radius of Na^+ (1.02 Å) compared to Li^+ (0.76 Å), the reaction kinetics of SIBs is sluggish with severe volume changes. [3,4,7-10] Two-dimensional (2D) transition metal sulfides with high theoretical specific capacity (670 mAh g^{-1} for MoS_2) and tunable interlayer spacing have widely been investigated as desirable anode materials for SIBs. [11-16] However, the inadequate charge/mass transfer, [15] and large volume variation during the charge/discharge cycling tends to deteriorate cycling stability and high-rate performance. [17,18] To solve these issues, strategies on modulation of microstructure, expansion of interlayer distance, as well as incorporation with various conductive matrixes, have been employed. [3,17,19-21]

Amphiphilic molecules and polymers such as cetyltrimethylammonium bromide (CTAB), oleylamine, oleic acid, and polyvinyl pyrrolidone (PVP) have been used as expander and/or carbon precursors to synthesize large interlayer space or single layered MoS_2/carbon composites to improve their electrochemical kinetics and structural stability. [2,22-26] Wang *et al.* [18] prepared a three-dimensional MoS_2 nanoflowers with an expanded interlayer spacing on double layer carbon tubes with the assistance of PVP. Zhu *et al.* prepared a single layered ultra-small nanoplates of MoS_2 embedded in carbon nanofibers by an electrospinning process. [26] Mesoporous materials with large specific surface area, narrow pore size distribution and large pore volume offer abundant active sites and efficient mass/charge transfer for sodium storage. Traditionally, ordered mesoporous metal sulfides and selenides materials are synthesized by using ordered mesoporous silica as hard template (e.g. Pluronic P123 for SBA-15). [27-31] Normally, the organic templates (such as Pluronic P123 for SBA-15) are removed by calcination or other methods before the mesoporous silica are used as hard-templates. However, the as prepared mesoporous silica with the organic templates are

still inside the pore channels are seldom be used directly as templates due to their pore channels are blocked. Unexpectedly, the nitrogen sorption results (Figure S1) of the untreated SBA-15 (with P123 still inside, named as SBA-15-P123) show that it already has an open pore framework with considerable specific surface and pore volume. These features make it a potential hard template.

We herein report a versatile dual-templates strategy to fabricate single layered mesoporous transition metal sulfide/carbon composites by using SBA-15-P123 as the template. The mesostructured silica framework provides a confined space to prevent the metal sulfides from growth outside the channels. While Pluronic P123 polymer serves a matrix to facilitate the metal sulfides precursor highly dispersed and acts as the carbon source. The dual-templates strategy avoids the use of additional carbon source, and poisonous sulfur source (such as S, H_2S), resulting in an eco-friendly and controllable process. Specifically, single layered mesoporous MoS_2/carbon materials (denoted as SMSC-x-Mo-y, where x represents the template (1 represent SBA-15-P123, 2 for MCF-P123, 3 for KIT-6-P123, 4 for MCM-41-CTA$^+$ and 5 for pure P123) and y represent different metal sulfide loading amounts) are constructed with the MoS_2 loading up to 80 wt% and surface area up to 237 m^2 g^{-1}. The detailed physicochemical properties of all the composites are summarized in Table S1. When evaluated as an anode material for SIBs, the SMSC-1-Mo-2 shows excellent cycling stability and outstanding high-rate performance. Furthermore, this method is also suitable for synthesizing other two-dimensional metal sulfide/carbon composites such as WS_2 and ReS_2 with potential applications such as energy storage, [11] catalysis, [31] biomedicine, [32] and sensor. [33]

2. Results and Discussion

As illustrated in **Figure 1**a, thiourea is mixed with SBA-15-P123. Then, $H_3PMo_{12}O_{40}$ (PMA) is added to the mixed solution during magnetic stirring. After the solvent evaporated, thiourea and PMo_{12}^-

4

are impregnated into the pore of silica template. Owing to the existence of thiourea, there is no need to add extra harmful sulfur vapor and/or H_2S gas at the following vulcanization process in Ar atmosphere. As the temperature increased, P123 is pyrolyzed and simultaneously intercalated into the layer space of MoS_2 nanosheets. Finally, after template removal, a series
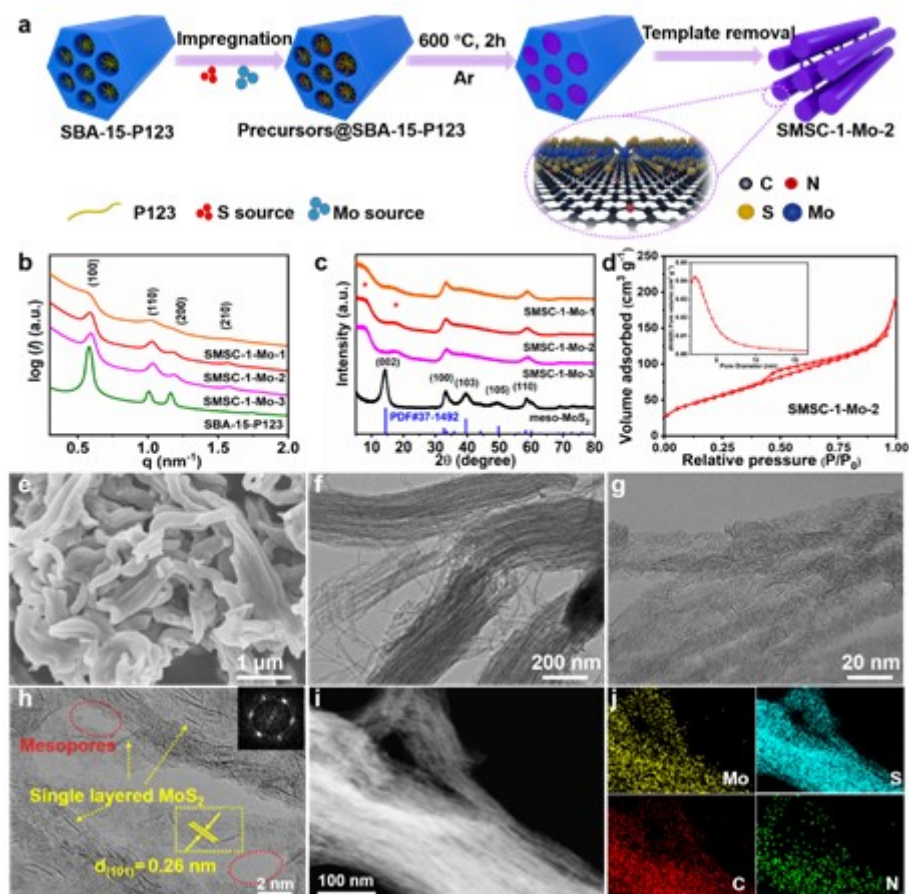
Figure 1. a) Schematic illustration of the formation process of SMSC-1-Mo. b) SAXS patterns. c) XRD patterns. d) N_2 adsorption/desorption isotherms and pore size distribution of SMSC-1-Mo-2. e) SEM image, f,g) TEM images, h) HRTEM image, i) STEM image and j) corresponding elemental mappings of SMSC-1-Mo-2.

of single layered mesoporous MoS_2/C composites (SMSC-1-Mo-1, SMSC-1-Mo-2, SMSC-1-Mo-3) with the carbon content of 30, 26 and 20% are formed. The carbon contents are determined by thermogravimetric analysis (TGA) (Figure S2). Pure P123 and SBA-15-OH (silanol-rich SBA-15) [34] are also used as templates for the synthesis. Single layered MoS_2 is also observed in the transmission electron microscopy (TEM image) of SMSC-5-Mo by only using P123 as the soft-template and carbon source (Figure S3). Single layered MoS_2 is absent by using SBA-15-OH as the template (named as meso-MoS_2, Figure S4). TEM image of meso-MoS_2 shows an interlayer spacing of 0.65 nm (Figure S4b), indicating that P123 plays an important role in formation of single layer MoS_2 structure. The carbon content of annealed thiourea@SBA-15-P123 is 7.7 % (Figure S5 and S6). When annealing SBA-15-P123 without impregnating thiourea in Ar, P123 is completely decomposed and there is almost no residual carbon. The thiourea may facilitate the carbonization process of P123 to a certain degree. Thus, the P123 is pyrolyzed and simultaneously intercalated into the inter layer space of MoS_2 sheets during the formation of MoS_2.

Small angle X-ray scattering (SAXS) patterns of all the SMSC-1-Mo samples in Figure 1b clearly show four well-resolved scattering peaks that can be ascribed to (100), (110), (200), and (210) planes of two dimensional (2D) hexagonal symmetry with the space group of *p*6*mm*, indicating good replication of the ordered mesoporous silica template. Powder X-ray diffraction (XRD) patterns (Figure 1c) of meso-MoS_2 shows distinct reflections of 2H phase MoS_2 (JCPDS No. 37-1492). While the (002) reflection peak of all the SMSC-1-Mo composites disappears, suggesting no stacking of MoS_2 layers in the *c* direction. Beside the two reflection peaks at 33.5° and 59.1° of (100) and (110) planes of MoS_2, the SMSC-1-Mo composites also display two weak reflections at ~7.5° and 17.6°, which are attributed to the reflection from adjacent single layered MoS_2 sheets. [18,20,23,26] These two peaks shift to lower degree positions with the decreasing of MoS_2 content, indicating higher single layered MoS_2 content formed. [35-37] As shown in Figure 1d and Figure S7a, the nitrogen

6

adsorption-desorption isotherm of SMSC-1-Mo-2 and the other two composites have two distinguishable capillary condensation steps, coinciding with a type IV isotherm. The Brunauer-Emmet-Teller (BET) surface areas of SMSC-1-Mo-1, SMSC-1-Mo-2, and SMSC-1-Mo-3 are calculated to be 237, 190 and 182 $m^2 g^{-1}$. The pore volumes are 0.39, 0.29 and 0.22 $cm^3 g^{-1}$ (shown in Table S1). Scanning electron microscopy (SEM) (Figure 1e) image of SMSC-1-Mo-2 shows a rod-like morphology which analogous to the SBA-15 template. TEM (Figure 1f and g) images confirm the 2D hexagonal structure and single layered MoS_2 sheets occur. High-resolution TEM (HRTEM) image (Figure 1h) clearly shows the lattice of MoS_2 sheet. The interplane spacing is ~0.26 nm, consistent well with (101) crystal plane of 2H phase of MoS_2. The Fast Fourier Transform (FFT) image displays a typical hexagonal lattice structure. Similar structures appear in SMSC-1-Mo-1 and SMSC-1-Mo-3 (Figure S8). Surprisingly, the element of N is detected besides Mo, S and C in SMSC-1-Mo-2 (Figure 1j) based on scanning transmission electron microscopy (STEM) (Figure 1i). Figure S9 shows the content of N is about 3.0 wt%, consistent well with the result of elemental analysis (Table S2).

Furthermore, Raman spectroscopy and X-ray photoelectron spectroscopy (XPS) were carried out to analyze the chemical composition of SMSC-1-Mo-2 and meso-MoS_2. As shown in Figure 2a, the bands of 383-385 and 407-411 cm^{-1} are assigned to in-plane E^1_{2g} and out-of-plane A_{1g} vibrational modes of MoS_2. The frequency separation between E^1_{2g} and A_{1g} modes of SMSC-1-Mo-2 (23.4 cm^{-1}) is much lower than that of meso-MoS_2 (26.8 cm^{-1}), suggesting an enlarged layer spacing of SMSC-1-Mo-2. [18,20] The relative intensity ratio (I_D/I_G) values of D and G peaks is 0.78 for SMSC-1-Mo-2, demonstrating the existence of amorphous carbon. [5,38] The full-scan XPS spectra (Figure S10a) also indicate the existence of Mo, S, C, N and O elements both in SMSC-1-Mo-2 and meso-MoS_2. The above residual carbon and N-doping in the samples originate from the pyrolysis of P123 and decomposition of thiourea. As shown in the high-resolution XPS spectra of Mo 3d and S 2p (Figure 2b), the two peaks of SMSC-1-Mo-2 at ~232.6 and 229.4 eV are attributed to Mo^{4+} in the 2H

MoS$_2$. [20] Meanwhile, the peaks at ~161.8 and 162.9 eV are assigned to S 2P$_{3/2}$ and S 2P$_{1/2}$. [20,39] Compared to meso-MoS$_2$, the characteristic peaks of Mo^{4+} and S 2p for SMSC-1-Mo-2 shift toward the lower binding energy, indicating increased electron cloud density in the vicinity of MoS$_2$. [40] As depicted in Figure 2c, the high-resolution XPS spectrum of N 1s in SMSC-1-Mo-2 is divided into five peaks, including graphitic N (400.7 eV), pyrrolic N (399.7 eV), pyridinic N (398.1 eV), N-Mo band (396.2 eV), and Mo 3p (394.8 eV). Besides, the peak of N-Mo band at about 396.1 eV also appears in meso-MoS$_2$. [41] N-doping boosts the electrical conductivity, beneficial to electrochemical performance. [41-44]

The effects of N-doping on the MoS$_2$ structures are demonstrated by X-ray absorption near-edge structure (XANES) and extended X-ray absorption fine structure (EXAFS) spectra. The average valence of Mo species is proportional to valence photon energy, representing that the species with higher oxidation state has a higher absorption threshold position. [35] Figure 2d
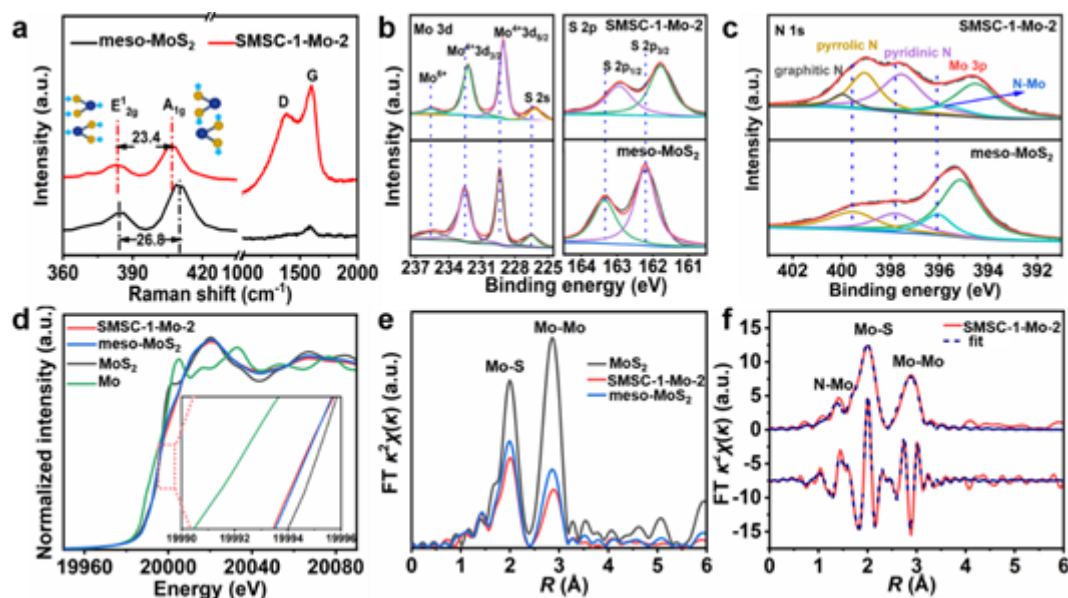
Figure 2. a) Raman spectra of SMSC-1-Mo-2 and meso-MoS$_2$. b) XPS spectra of the Mo 3d and S 2p regions, and c) N 1s region with fitting curves for SMSC-1-Mo-2 and meso-MoS$_2$, respectively. d)

8

XANES and e) Fourier-transformed Mo K-edge EXAFS spectra of pristine MoS$_2$, SMSC-1-Mo-2, and meso-MoS$_2$. f) R space Mo K-edge EXAFS spectra of SMSC-1-Mo-2.

shows that the absorption edge of meso-MoS$_2$ and SMSC-1-Mo-2 shift to high energy compared with Mo foil, representing that the Mo species in the meso-MoS$_2$ and SMSC-1-Mo-2 composite have higher oxidation state. The absorption threshold position of SMSC-1-Mo-2 (19993.4 eV) and meso-MoS$_2$ (19993.5 eV) are slightly lower than that of MoS$_2$ (19994.0 eV). This suggests that the Mo species have a lower Mo valence. The change of valence is caused by the formation of N-doping, which is further confirmed by EXAFS. [35,45] The SMSC-1-Mo-2 and meso-MoS$_2$ have smaller Mo-S (2.0 Å) and Mo-Mo (2.8 Å) peaks in Figure 2e, ascribed to the N-doping (see Figure 2f) and defects in the MoS$_2$. [35,45-47] The coordination number of Mo-N in SMSC-1-Mo-2 and meso-MoS$_2$ are 1.002 and 0.89. The detailed structural parameters, including coordination number and bond distance of the aforesaid samples, are illustrated in Figure S11 and Table S3. These observations further confirm that the N atoms are successfully doped into the MoS$_2$ crystal.

Electrochemical performances of the above samples are investigated as the anode material for SIBs. The first cathodic scan in cyclic voltammetry (CV) (Figure S12c) of meso-MoS$_2$ electrode shows three reduction peaks at about 1.31, 0.75 and 0.36 V, attributed to the intercalation of Na$^+$ into the MoS$_2$ layers, the conversion of Na$_x$MoS$_2$ to Na$_2$S and Mo, as well as the electrolyte decomposition and formation of solid electrolyte interfaces (SEI), respectively. [1,3,48] The reduction peak of SMSC-1-Mo-2 at about 1.3 V is almost disappeared (Figure 3a). It implies that the intercalation reaction of Na$^+$ into MoS$_2$ nanosheets is minor. Instead, Na$^+$ might be adsorbed on the surface of single layered MoS$_2$ by the interfacial storage mechanism, which is a typical capacitively controlled charge storage behavior. [8] Such feature has been proved to impart fast kinetic and long durability to

electrode materials. [1,8] In the subsequent scans, the feature related with SEI film gradually disappears from the CV curves. Owing to the irreversible capacity loss caused by the formation of SEI film, the area of CV curve for the first scan is dramatically decreased. The subsequent two curves after the first cycle almost overlap, indicating a stable surface state, structure and electrochemical reversibility after the initial activation process. [48-50] Owing to the identical chemical composition, CV profiles of SMSC-1-Mo-1 (Figure S12a) and SMSC-1-Mo-3 (Figure S12b) are nearly the same to that of SMSC-1-Mo-2, demonstrating similar sodium storage mechanism.

Figure 3b and Figure S12d-f display the discharge-charge voltage profiles of different electrodes for the first three cycles. The initial Coulombic efficiencies (ICEs) are ~55, 42, 62, and 47 %, respectively. While, the ICE of mesoporous carbon (MC) electrode in FigureS13 is only ~17%. The irreversible capacity loss for the first cycle is attributed to the irreversible formation of SEI film, which is commonly known as the electrochemical activation. [12,13] Owing to the large specific surface area of the above samples and the introduction of carbon matrix, the decomposition of electrolyte and irreversible trapping of Na^+ in the composite could lead to considerable side reactions. It is also responsible for the low ICE. [49-50] Among different electrodes in Figure 3c, SMSC-1-Mo-2 electrode shows the highest specific capacities of 530, 490, 470, 450, 430, 400 and 370 mAh g^{-1} at 0.05, 0.1, 0.2, 0.5, 1, 2, and 4 A g^{-1}, respectively.
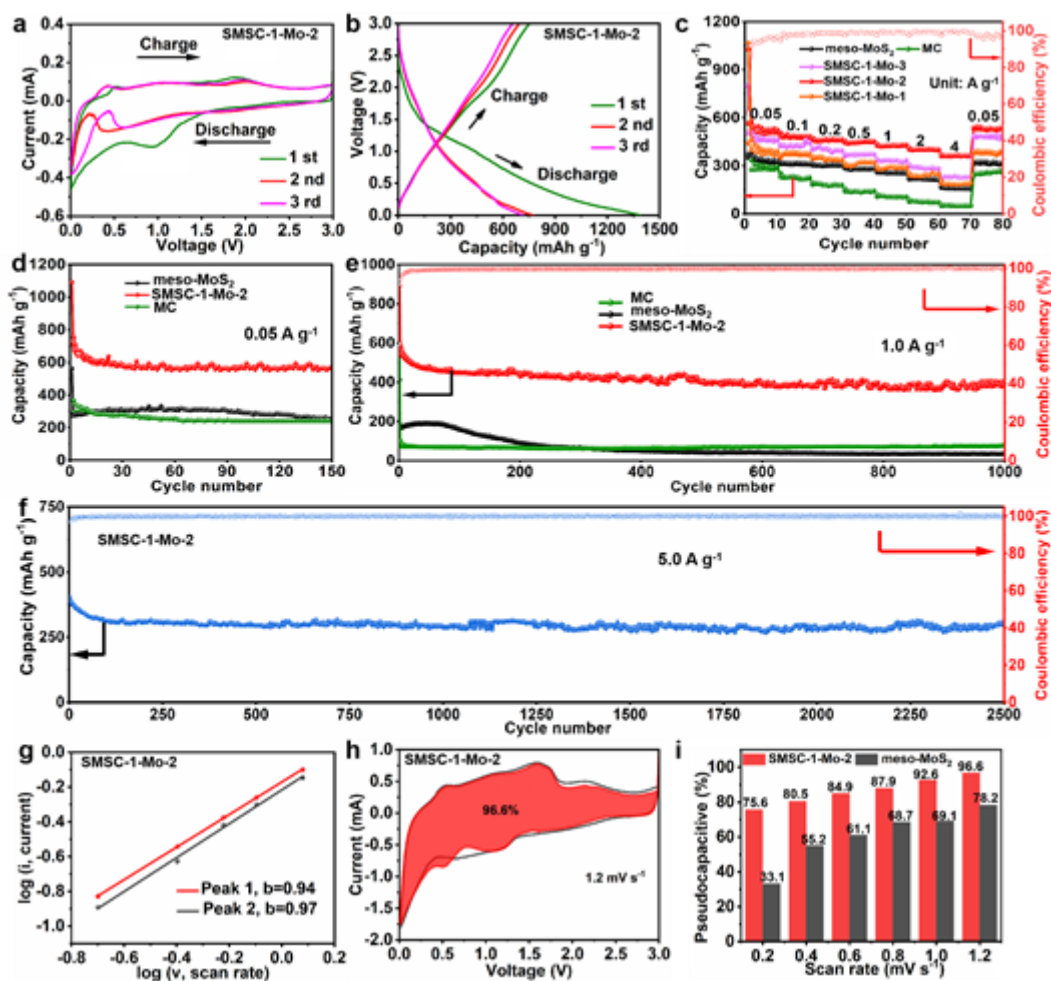
Figure 3. Electrochemical performance for SIBs. a) CV curves and b) the first three-cycle discharge and charge profiles of SMSC-1-Mo-2 electrode. b) Rate capabilities of SMSC-1-Mo-1, SMSC-1-Mo-2, SMSC-1-Mo-3, MC and meso-MoS$_2$ electrodes. d,e) Cycling performances of SMSC-1-Mo-2, MC and meso-MoS$_2$ electrodes at 0.05 and 1.0 A g^{-1}, respectively. f) Long cycle performance of SMSC-1-Mo-2 at 5.0 A g^{-1}. g) The plot of log (scan rate) versus log (peak current) for anodic and cathodic peaks, h) CV profile with the capacitive contribution at scan rate of 1.2 mV s^{-1} of SMSC-1-Mo-2 electrode, respectively. i) Capacitive contribution at different scan rates for SMSC-1-Mo-2 and meso-MoS$_2$ electrodes.

When the current density reduces to 0.05 A g^{-1}, the specific capacity of SMSC-1-Mo-2 (~535 mAh g^{-1}) is slightly higher than the initial value. The CE of SMSC-1-Mo-2 in Figure 3c gradually increases to stable value (usually near 100%) from a low value in the very first several cycles. This phenomenon is usually ascribed to the formation of a stable electrode interface (SEI) because a dense SEI can effectively avoid considerable side reactions and accordingly achieve a high CE after several cycles. [12,13,49-54] Figure 3d manifests the cycling performances of the above electrodes at 0.05 A g^{-1}. After 150 cycles, SMSC-1-Mo-2 electrode displays a much higher specific capacity of 570 mAh g^{-1} than that of meso-MoS$_2$ (260 mAh g^{-1}) and MC (240 mAh g^{-1}) electrodes. When the current density reaches to 1.0 A g^{-1}, SMSC-1-Mo-2 delivers a higher reversible capacity of 385 mAh g^{-1} after 1000 cycles (Figure 3e). Compared with SMSC-1-Mo-2, meso-MoS$_2$ initially shows a stable cycling performance with a lower capacity of ~200 mAh g^{-1} before 75th cycle and then undergoes fast capacity fading to ~40 mAh g^{-1} after 1000 cycles. This phenomenon suggests that meso-MoS$_2$ electrode suffers from the large volume change-induced uncontrolled aggregation. The capacity of MC electrode is only ~80 mAh g^{-1} after 1000 cycles. The significant cycling difference among the above electrodes implies better mechanical stability and superior electrochemical performance of SMSC-1-Mo-2. SMSC-1-Mo-2 maintains a much higher capacity of 310 mAh g^{-1} even at 5.0 A g^{-1} after 2500 cycles (Figure 3f). Compared with other MoS$_2$-based electrodes in related literatures (Table S4), SMSC-1-Mo-2 electrode still has great advantages in terms of reversible capacity and cycle stability.

As shown in Figure S14, the area surrounded by the CV curves represents the total amount of sodium storage during the electrochemical reaction, including capacitive and diffusion contribution. The proportion of the capacitive contribution is revealed according to the equations as follows:

$$i=av^{b} \tag{1}$$

$$log\ (i) = log\ (a) + b\ log\ (\upsilon) \tag{2}$$

Among them, b value is the slope of linear fitting line of the log (i) and log (υ) value. If the b value approaches to 1.0, a capacitive-controlled process dominates the storage behavior. [53] The b values of SMSC-1-Mo-2 (Figure 3g) and meso-MoS$_2$ (Figure S15b) are 0.94 (peak 1)/0.97 (peak 2) and 0.99 (peak 1)/0.85 (peak 2), suggesting capacitive-controlled process occupies a dominant contribution for sodium storage kinetics. The capacitive contribution can be further calculated according to the following equation:

$$i=k_1\upsilon+k_2\upsilon^{1/2} \tag{3}$$

The coefficient k_1 and k_2 are related to the contribution of capacitive and ion diffusion, respectively. As shown in Figure 3h, when the scan rate reaches 1.2 mV s^{-1}, the capacitive contribution in SMSC-1-Mo-2 reaches 96.6%, indicating most of the capacity contribution originates from the surface of the composite. Compared with meso-MoS$_2$, the higher capacitive contribution in SMSC-1-Mo-2 (Figure 3i) is mainly attributed to the following structural advantages: 1) the single layered structure can rationally shorten ion diffusion pathways and decrease the Na$^+$ barrier to facilitate fast charge carrier transport; 2) the introducing carbon matrix leads to rapid electron transfer within the entire electrode; 3) the large specific surface area provides sufficient active area for adsorption and desorption of Na$^+$, thus leading to an excellent rate performance for SMSC-1-Mo-2. [8,13,53,54]

Electrochemical impedance spectroscopy (EIS, Figure S16) experiments show that the charge transfer resistances both before and after 150 cycles of SMSC-1-Mo-2 are much lower than those of the meso-MoS$_2$ electrode. The result further demonstrates the superior electronic conductivity and fast Na$^+$ kinetic diffusion in the solid materials, as well as the enhanced capacitive-like storage behavior of SMSC-1-Mo-2 during cycling. [50,53] In order to further study the reaction kinetics of

$$D_{Na^+} = \frac{4}{\tau\pi}\left(\frac{m_B V_M}{M_B S}\right)^2\left(\frac{\Delta E_S}{\Delta E_\tau}\right)^2$$

13

SMSC-1-Mo-2 and meso-MoS$_2$ anodes, the galvanostatic intermittent titration technique (GITT) test is shown in Figure S17a. According to Fick' second law: [13,54]

$$(4)$$

where τ, m_B, M_B, V_M, and S stand for the time of current pulse (s), the mass, the molar mass, the molar volume of active materials, and the area of electrode, respectively. The calculation of ΔE_S and $\Delta E\tau$ are displayed in Figure S17b. Figure S17 (c,d) show that the diffusion coefficient of Na$^+$ for SMSC-1-Mo-2 electrode is slightly higher than that of meso-MoS$_2$, suggesting faster Na$^+$ diffusivity in SMSC-1-Mo-2.

14
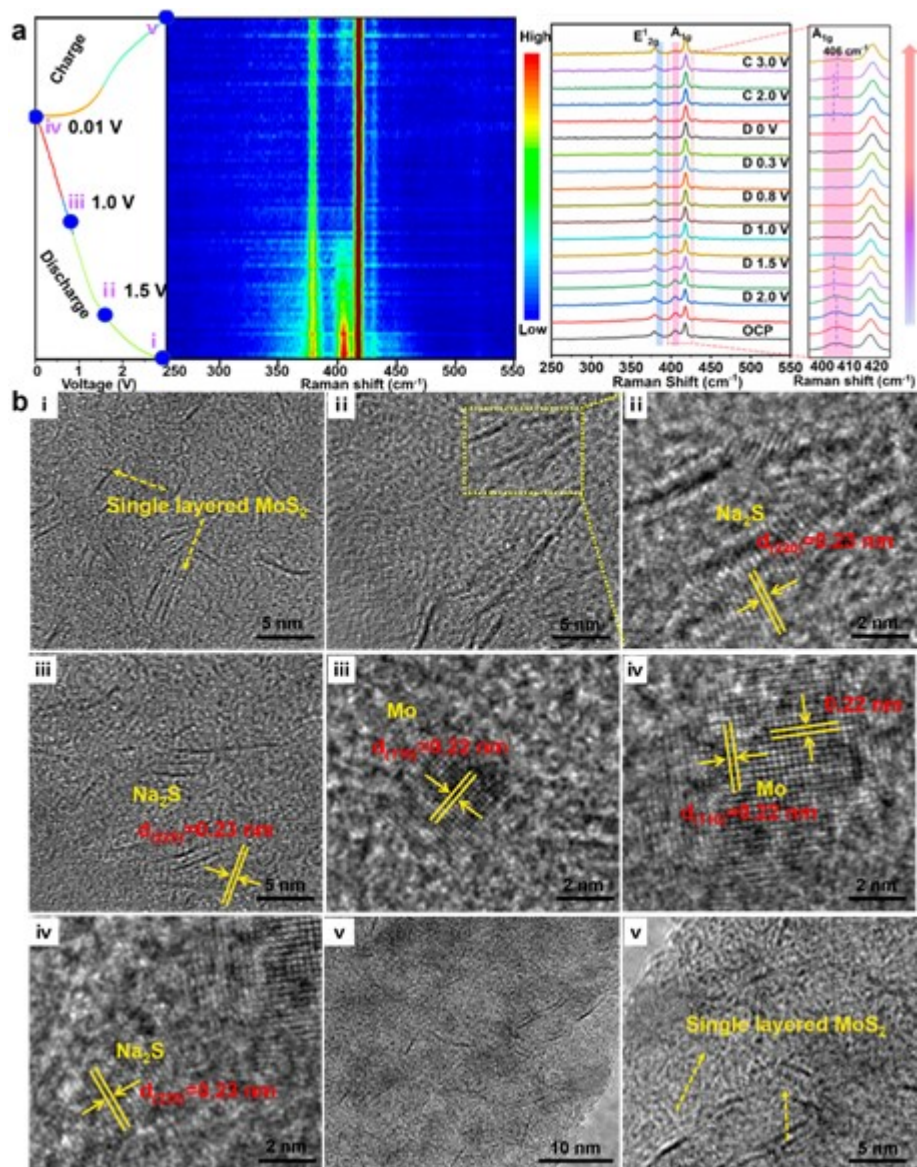
Figure 4. Structure evolution on Na⁺ extraction/insertion. a) *In situ* Raman test of SMSC-1-Mo-2 for the first cycle. b) Corresponding *ex situ* HRTEM images of SMSC-1-Mo-2 electrode at different stages of the first cycle.

Figure 4a shows *in situ* Raman result of SMSC-1-Mo-2 for the first cycle. Along with the discharging process, the peaks of A_{1g} (~406 cm^{-1}) and E^1_{2g} (~384 cm^{-1}) gradually attenuate. As the voltage reduces from open circuit potential (OCP) to 0.8 V, the two peaks almost disappear. This situation remains the same until 0.01 V. During the charging process, the aforesaid two peaks gradually appear at about 1.5 V and become more apparent when the voltage increases to 3.0 V, indicating the reappearance of MoS$_2$. According to the detailed diagram of *in situ* Raman spectra from 395 to 425 cm^{-1}, A_{1g} peak has a slight shift, indicating the unobvious Na$^+$ intercalation/deintercalation process, which agrees well with the CV curves of SMSC-1-Mo-2. This phenomenon is ascribed to the single layered MoS$_2$ which has enough layer space to rapidly adsorb Na$^+$.[1,8] There is almost no significant shift in the position of the two peaks after cycling, further explaining the extraordinary structural stability of SMSC-1-Mo-2.

The corresponding *ex situ* HRTEM images in Figure 4b illustrate the phase transformation of SMSC-1-Mo-2 at different stages. During Na$^+$ insertion, the crystal structure of single layered MoS$_2$ weakens and discharging product (Na$_2$S) appears, indicating the conversion reaction taking place at the voltage of 1.5 V. Owing to the more active sites in single layered MoS$_2$ are directly exposed than that in multi-layer MoS$_2$, the SMSC-1-Mo-2 electrode achieves a rapid Na$^+$ intercalation/de-intercalation and thereby receives an enhanced rate capability. Along with the discharging process going on to 0.01 V, single layered MoS$_2$ nanosheets nearly disappears and is mainly converted to Na$_2$S and Mo. When the voltage increases to 3.0 V, the single layered MoS$_2$ nanosheets reappear, revealing the excellent reversibility of SMSC-1-Mo-2 anode. The corresponding TEM images in Figure S18 further illustrate the single layered MoS$_2$ nanosheets periodically disappear/appear upon cycling. Slight nanoparticles also appear after cycling. According to the HRTEM analysis in Figure S18, the nanoparticles might be Na$_2$S, generated from the conversion reaction. These Na$_2$S nanoparticles also disappear/appear periodically upon cycling.[55]

The morphology of SMSC-1-Mo-2 in Figure S19 (a,b) is well-maintained after 150 cycles. In addition, owing to the existence of the amorphous carbon, the severe aggregation in single layered MoS_2 materials during repeated cycling is significantly alleviated, leading to the superior high-rate capability and excellent long-term cycle stability.

DFT (Figure 5) calculations reveal the models of Na adsorption on single MoS_2 and MoS_2/graphene (MoS_2-G (002)) surface. The adsorption energy of Na on MoS_2-G (002) is -1.80 eV, much higher than that (-1.50 eV) on MoS_2. The higher adsorption energy indicates that Na can be more easily anchored on the MoS_2-G (002) configuration than the single MoS_2, resulting in higher Na storage ability in the former case. Such an enhanced ability for anchoring
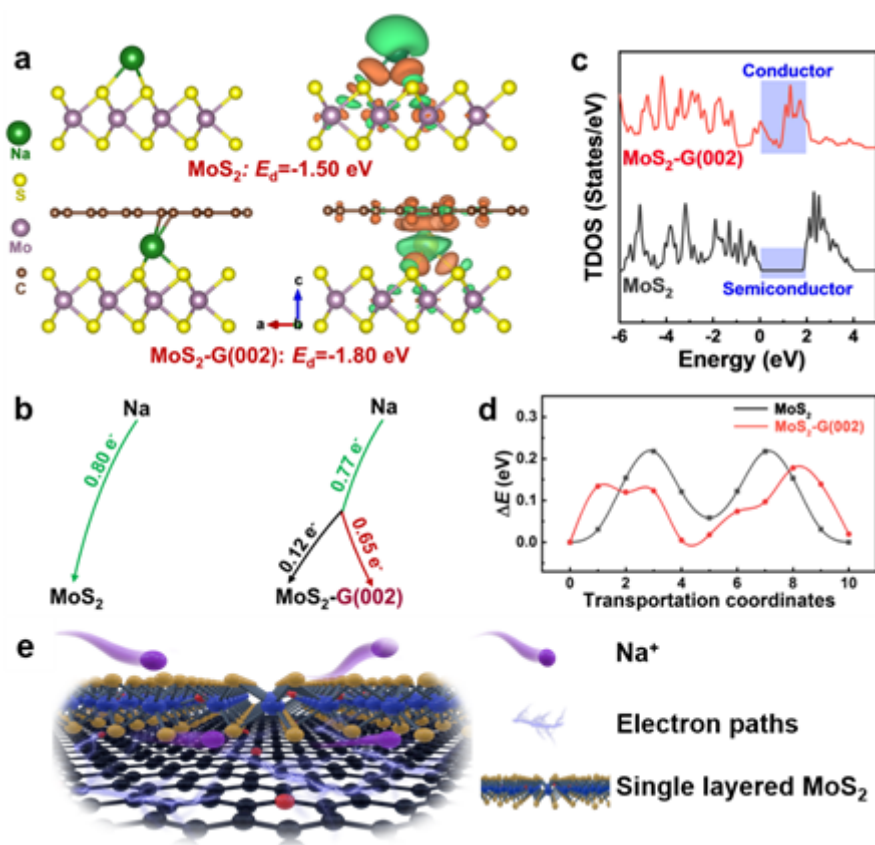
Figure 5. a) Optimized structures for the adsorption of Na on MoS_2 and MoS_2-G (002) as well as the corresponding isosurfaces of local charge density difference (Green and red denote -1.25×10^{-3} and 1.25×10^{-3} e^- per $Å^3$ isosurfaces, respectively). b) Bader charge analysis for determining the Electron transfer from Na to MoS_2 and MoS_2-G (002). c) Total density of states (TDOS) of MoS_2 and MoS_2-G (002). d) Migration energy of Na from one adsorption site to adjacent adsorption site. e) Schematic illustration of superior electrochemical performance of SMSC-1-Mo-2 composite.

Na results from the synergy effect between MoS_2 and graphene, which tunes the electron transfer ways around the Na atoms. Electron transfer occurs mainly between Na and S atoms for the MoS_2-Na (adsorption of Na on MoS_2) configuration, which means electrons of Na are lost and accumulated around the nearby S atoms (Figure 5a). Instead, the lost electrons of Na are allocated on both nearby S atoms of MoS_2 and adjacent C atoms of graphene for MoS_2-G (002)-Na configuration (adsorption of Na on MoS_2-G (002)). Tuning the electron transfer by addition of graphene is further revealed by the Bader charge analysis (Figure 5b). It means that the lost 0.80 e^- of Na are completely transferred to MoS_2 on the MoS_2-Na configuration, while the depleted 0.77 e^- of Na are distributed on both MoS_2 (0.12 e^-) and graphene (0.65 e^-) on the MoS_2-G (002)-Na configuration. Therefore, the existence of graphene on MoS_2 tunes the electrons transfer between Na and the composites, contributing to more easily anchoring of Na for SIBs. Another merit of adding graphene to the MoS_2 materials is the enhanced conductivity (Figure 5c), as shown by the change from the semiconductor-characteristic TDOS of MoS_2 to conductor-characteristic TDOS of MoS_2-G (002). The increased conductivity accelerates the charge transfer. Moreover, the existence of graphene promotes the migration of Na atoms (Figure 5d), as shown by the lower migration barriers of Na on MoS_2-G (002) than that on MoS_2. This promotion results in fast reaction kinetics and excellent electrochemical performance. The DFT calculations and the experiment results all

18

demonstrate that the superior electrochemical performance of SMSC-1-Mo-2 is mainly attributed to its highly predominated charge storage mechanism of the capacitive process. As illustrated in Figure 5e, the incorporation of carbon on MoS2 sheet surface promotes the Na storage and charge transfer.
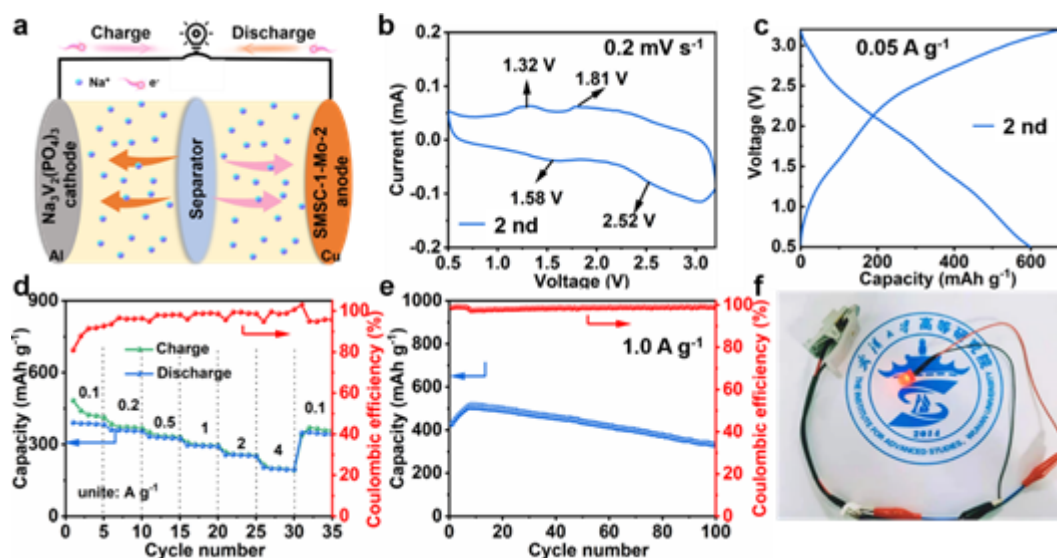
Figure 6. Electrochemical performance of sodium ion full batteries. a) Schematic illustration of assembling sodium ion full battery (SMSC-1-Mo-2//NVP) with SMSC-1-Mo-2 and NVP as anode and cathode, respectively. b) CV and c) charge-discharge curves of SMSC-1-Mo-2//NVP at 2nd cycle. d) Rate capability and e) cycling performance of SMSC-1-Mo-2//NVP in the cut-off voltage of 0.5-3.2 V. f) Optical image of the sodium ion full battery powering a LED bulb.

In view of the prominent performance of SMSC-1-Mo-2 electrode in half-cell, sodium ion full cells are constructed by using $Na_3V_2(PO_4)_3$ (NVP) as the cathode (**Figure 6**a). Before assembling the full cell, the SMSC-1-Mo-2 anode is pre-sodiated for 3 cycles to prevent the side reactions between the electrode and electrolyte. The ratio of cathode material (NVP) to anode material (SMSC-1-Mo-2) is

~6, calculated based on the charge capacities of SMSC-1-Mo-2 and NVP in Figure S20. Voltage cutoff window of SMSC-1-Mo-2//NVP is designed as 0.5-3.2 V for all of the charge-discharge processes. As shown in Figure 6b, two broad peaks at 1.58, 2.52 V in cathodic sweep and 1.32, 1.81 V in anodic sweep appear in the CV of the full cell. As shown in Figure 6c, the discharge and charge specific capacities are ~600 and 630 mA h g^{-1} with a CE of 95.2% at a current density of 0.05 A g^{-1} (based on the mass of SMSC-1-Mo-2). Figure 6d shows the rate capability of the SMSC-1-Mo-2//NVP from 0.1 to 4.0 A·g^{-1}. The average specific capacities of the SMSC-1-Mo-2//NVP are 394, 365, 337, 296, 251, 201 mAh g^{-1} at the current densities of 0.1, 0.2, 0.5, 1.0, 2.0, 4.0 A·g^{-1} after 5 cycles, respectively. Importantly, when the current density returned to 0.1 A·g^{-1}, the SMSC-1-Mo-2//NVP recovers to nearly 350 mAh·g^{-1}, indicating excellent rate performance. After 100 cycles at 1.0 A g^{-1} (Figure 6e), the specific capacity is retained ~330 mA h g^{-1}. In Figure 6f, an LED bulb is successfully lighted up by the assembled SMSC-1-Mo-2//NVP full cell. When compared to other MoS$_2$-based full cells in Table S5, the performance of SMSC-1-Mo-2//NVP full cell is also outstanding. The superior performance for both SIBs and full cells is ascribed to the following two aspects: (ⅰ) The incorporation of amorphous carbon, defects and N-doping, as well as the establishment of MoS$_2$-carbon heterointerface can enhance the electronic conductivity, increase numerous active sites for sodium storage, accelerate charge transfer, prevent the stacking of single layered MoS$_2$ nanosheets and thereby maintain the structural stability during the cycling; (ⅱ) Single layered MoS$_2$ and ordered mesoporous nanostructure can expose more active sites and accelerate the ion diffusion kinetics.

Apart from excellent performance, a security, eco-friendly, convenient and controllable method for unique materials is of great importance to practical application. In this work, to further demonstrate the generality of this method, different single layered mesoporous MS$_2$/C (M=Mo, W, Re) composites are successfully synthesized by using other mesoporous silica templates (e.g. MCF-P123, KIT-6-P123, MCM-41-CTA$^+$) and metal precursors (e.g. PMA, H$_3$PW$_{12}$O$_{40}$ and NH$_4$ReO$_4$). As

shown in Figure S21(a-c), single layered MoS_2 nanosheets occur in SMSC-2-Mo templated from MCF-P123, SMSC-3-Mo templated from KIT-6-P123, and SMSC-4-Mo templated from MCM-41-CTA[+], respectively. The XRD patterns of the above samples in Figure S21(d-f) also demonstrate the single layered MoS_2, consistent with the TEM images. The XRD pattern of SMSC-1-W templated from SBA-15-P123 in Figure S22a shows no crystal plane diffraction peak appearance at 14.4°, indicating there is no stack along (002) plane, and thus proving the sample is single layered WS_2 nanosheets. The result corresponds to its TEM image in Figure S22b. Similarly, taking the NH_4ReO_4 as the metal precursor, the single layered mesoporous ReS_2/C (SMSC-1-Re) templated from SBA-15-P123 is successfully obtained according to Figure S23, demonstrating the generality of this synthetic approach. The physicochemical properties of the above samples are also summarized in Table S1.

3. Conclusion

In summary, a versatile, eco-friendly, and general synthesis strategy has been developed to exclusively fabricate single layered mesoporous metal sulfide/carbon composite. The obtained MoS_2/carbon nanocomposites have a high specific surface area of up to 237 m^2 g^{-1} and high MoS_2 content of up to 80%. The unique single layered structure significantly promotes the electrical conductivity and structural stability. As expected, the SMSC-1-Mo-2 displays a remarkable electrochemical performance with prolonged cycle life, superior reversible capacity and excellent rate capability. Besides, the reaction mechanism of SMSC-1-Mo-2 has been systematically investigated by *in situ* and *ex situ* characterizations. This work could be expected to guide the future designing protocol for various mesoporous single layered transition metal sulfide/carbon composite materials.

WILEY-VCH

Supporting Information

Supporting Information is available from the Wiley Online Library or from the author.

Received: ((will be filled in by the editorial staff))
Revised: ((will be filled in by the editorial staff))
Published online: ((will be filled in by the editorial staff))

References

[1] K, Ma. H, Jiang. Y. J. Hu, C. Z. Li, *Adv. Funct. Mater.* **2018**, *28*, 1804306.

[2] D. L. Chao, P. Liang, Z. Chen, L. Y. Bai, H. Shen, X. Liu, X. H. Xia, Y. L. Zhao, S. V. Savilov, J. Y. Lin, Z. X. Shen, *ACS Nano* **2016**, *10*, 10211.

[3] Q. C. Pan, Q. Zhang, F. Zheng, Y. Liu, Y. Li, X. Ou, X. Xiong, C. Yang, M. Liu, *ACS Nano* **2018**, *12*, 12578.

[4] Q. N. Liu, Z. Hu, Y. R. Liang, L. Li, C. Zou, H. L. Jin, S. Wang, H. M. Lu, Q. F. Gu, S. L. Chou, Y. Liu, S. X. Dou, *Angew. Chem. Int. Ed.* **2020**, *59*, 5159.

[5] C. Wu, P. Kopold, P. A. van Aken, J. Maier, Y. Yu, *Adv. Mater.* **2017**, *29*, 1604015.

[6] Y. T. Feng, M. Z. Xu, T. He, B. J. Chen, F. Gu, L. H. Zu, R. J. Meng, J. H. Yang, *Adv. Mater.* **2021**, 2007262.

[7] S. P. Zhang, G. Wang, B. B. Wang, J. M. Wang, J. Y. Bai, H. Wang, *Adv. Funct. Mater.* **2020**, *30*, 2001592.

[8] H. Qi, L. Y. Cao, J. Y. Li, J. F. Huang, Z. W. Xu, Y. Y. Cheng, X. G. Kong, K. Yanagisawa, *ACS Appl. Mater. Interfaces* **2016**, *8*, 35253.

[9] J. F. Ruan, F. Mo, Z. Long, Y. Song, F. Fang, D. Sun, S. Zheng, *ACS Nano* **2020**, *14*, 12222.

[10] W. Wang, B. Jiang, C. Qian, F. Lv, J. Feng, J. Zhou, K. Wang, C. Yang, Y. Yang, S. Guo, *Adv. Mater.* **2018**, *30*, 1801812.

[11] L. H. Lv, W. W. Lei, S. Liu, W. H. Zhang, *Adv. Electron. Mater.* **2019**, *5*, 1800830.

[12] F. Zhou, S. Xin, H. W. Liang, L. T. Song, S. H. Yu, *Angew. Chem. Int. Ed.* **2014**, *53*, 11552.

[13] M. Z. Ma, S. P. Zhang, Y. Yao, H. Y. Wang, H. J. Huang, R. Xu, J. W. Wang, X. F. Zhou, W. J. Yang, Z. Q. Peng, X. J. Wu, Y. L. Hou, Y. Yu, *Adv. Mater.* **2020**, *32*, 2000958.

[14] Q. Pang, Y. Gao, Y. Y. Zhao, Y. M. Ju, H. L. Qiu, Y. J. Wei, B. B. Liu, B. Zou, F. Du, G. Chen, *Chemistry* **2017**, *23*, 7074.

[15] S. C. Liang, S. Zhang, Z. Liu, J. Feng, Z. Jiang, M. J. Shi, L. Chen, T. Wei, Z. J. Fan, *Adv. Energy Mater.* **2021**, *11*, 2002600.

[16] Z. Hu, L. X. Wang, K. Zhang, J. B. Wang, F. Y. Cheng, Z. L. Tao, J. Chen, *Angew. Chem., Int. Ed.* **2014**, *53*, 12794.

[17] L. L. Wang, H. T. Zhang, Y. L. Wang, C. Qian, Q. Dong, C. H. Deng, D. F. Jiang, M. Y. Shu, S. S. Pan, S. J. Zhang, *J. Mater. Chem. A* **2020**, *8*, 15002.

[18] Y. H. Wang, Y. Yang, D. Y. Zhang, Y. B. Wang, X. K. Luo, X. M. Liu, J. K. Kim, Y. S. Luo, *Nanoscale Horiz.* **2020**, *5*, 1127.

[19] P. Song, J. Di, L. X. Kang, M. Z. Xu, B. J. Tang, J. Xiong, J. W. Cui, Q. S. Zeng, J. D. Zhou, Y. M. He, Q. D. Fu, J. Peng, S. S. Guo, B. Lin, J. Y. Zhang, P. Meng, Z. Liu, *Nano Mater. Sci.* **2019**, *1*, 310.

[20] B. Q. Xie, Y. Chen, M. Y. Yu, T. Sun, L. H. Lu, T. Xie, Y. Zhang, Y. C. Wu, *Carbon*, **2016**, *99*, 35.

[21] S. W. Li, Y. C. Liu, X. D. Zhao, Q. Y. Shen, W. Zhao, Q. W. Tan, N. Zhang, P. Li, L. F. Jiao, X. H. Qu, *Adv. Mater.* **2021**, *33*, 2007480.

[22] Y. P. Pang, M. N. Uddin, W. Chen, S. Javaid, E. Barker, Y. G. Li, A. Suvorova, M. Saunders, Z. Y. Yin, G. H. Jia, *Adv. Mater.* **2019**, 1905540.

[23] Z. Wang, T. Chen, W. X. Chen, K. Chang, L. Ma, G. C. Huang, D. Y. Chen, J. Y. Lee, *J. Mater. Chem. A* **2013**, *1*, 2202.

[24] S. K. Park, J. Lee, S. Bong, B. Jang, K. D. Seong, Y. Piao, *ACS Appl. Mater. Interfaces* **2016**, *8*, 19456.

[25] B. R. Jia, Y. Z. Zhao, M. L. Qin, W. Wang, Z. W. Liu, C. Y. Lao, Q. Y. Yu, Y. Liu, H. W. Wu, Z. L. Zhang, X. H. Qu, *J. Mater. Chem. A* **2018**, *6*, 11147.

[26] C. Zhu, X. Mu, P. A. van Aken, Y. Yu, J. Maier, *Angew. Chem., Int. Ed.* **2014,** *53*, 2152.

[27] X. P. Fang, X. Q. Yu, S. F. Liao, Y. F. Shi, Y. S. Hu, Z. X. Wang, G. D. Stucky, L. Q. Chen, *Microporous Mesoporous Mater.* **2012**, *151*, 418.

[28] H. Liu, D. W. Su, R. F. Zhou, B. Sun, G. X. Wang, S. Z. Qiao, *Adv. Energy Mater.* **2012**, *2*, 970.

[29] Y. F. Shi, C. X. Hua, B. Li, X. P. Fang, C. H. Yao, Y. C. Zhang, Y. S. Hu, Z. X. Wang, L. Q. Chen, D. Y. Zhao, G. D. Stucky, *Adv. Funct. Mater.* **2013**, *23*, 1832.

[30] F. J. Chen, J. Wang, B. Li, C. H. Yao, H. F. Bao, Y. F. Shi, *Mater. Lett.* **2014**, *136*, 191.

[31] W. M. Xu, K. J. Chai, Y. W. Jiang, J. B. Mao, J. Wang, P. F. Zhang, Y. F. Shi, *ACS Appl. Mater. Interfaces* **2019**, *11*, 17670.

[32] X. Zhang, Z. C. Lai, Z. D. Liu, C. L. Tan, Y. Huang, B. Li, M. T. Zhao, L. H. Xie, W. Huang, H. Zhang, *Angew. Chem. Int. Ed.* **2015,** *54*, 5425.

[33] B. M-Garcia, D. Spirito, S. Bellani, M. Prato, V. Romano, A. Polovitsyn, R. Brescia, R. O-Nunez, L. Najafi, A. Ansaldo, G. D'Angelo, V. Pellegrini, R. Krahne, I. Moreels, F. Bonaccorso, *Small* **2019,** *15*, 1904670.

[34] D. Gu, W. Schmidt, C. M. Pichler, H. J. Bongard, B. Spliethoff, S. Asahina, Z. W. Cao, O. Terasaki, F. Schüth, *Angew. Chem., Int. Ed.* **2017**, *56*, 11222.

[35] H. Wang, X. Xiao, S. Y. Liu, C. L. Chiang, X. Kuai, C. K. Peng, Y. C. Lin, X. Meng, J. Zhao, J. Choi, Y. G. Lin, J. M. Lee, L. Gao, *J. Am. Chem. Soc.* **2019**, *141*, 18578.

[36] W. S. Lee, E. Peng, T. A. Loh, X. Huang, J. M. Xue, *Nanoscale* **2016**, *8*, 8042.

[37] Y. C. Pang, S. Y. Zhang, L. M. Liu, J. Liang, Z. J. Sun, Y. K. Wang, C. H. Xiao, D. W. Ding, S. J. Ding, *J. Mater. Chem. A* **2017**, *5*, 17963.

[38] H. Chen, T. B. Song, L. B. Tang, X. M. Pu, Z. Li, Q. J. Xu, H. M. Liu, Y. G. Wang, Y. Y. Xia, *J. Power Sources* **2020**, *445*, 227271.

[39] S. K. Chong, L. Sun, C. Y. Shu, S. W. Guo, Y. N. Liu, W. Wang, H. K. Liu, *Nano Energy* **2019**, *63*, 103868.

[40] G. K. Veerasubramani, M. S. Park, G. Nagaraju, D. W. Kim, *J. Mater. Chem. A* **2019**, *7*, 24557.

[41] P. Tao, J. J. He, T. Shen, Y. Hao, J. K. Yan, Z. J. Huang, X. Xu, M. Li, Y. Chen, *Adv. Mater. Interfaces* **2019**, *6*, 1900460.

[42] R. M. Ding, M. C. Wang, X. F. Wang, H. X. Wang, L. C. Wang, Y. W. Mu, B. L. Lv, *Nanoscale* **2019**, *11*, 11217.

[43] F. Xiao, X. Yang, H. Wang, D. Y. W. Yu, A. L. Rogach, *ACS Appl. Mater. Interfaces* **2020**, *12*, 54644.

[44] S. Li, C. Cheng, A. Sagaltchik, P. Pachfule, C. Zhao, A. Thomas, *Adv. Funct. Mater.* **2019**, *29*, 1807419.

[45] J. T. Hu, L. Yu, J. Deng, Y. Wang, K. Cheng, C. Ma, Q. H. Zhang, W. Wen, S. S. Yu, Y. Pan, J. Z. Yang, H. Ma, F. Qi, Y. K. Wang, Y. P. Zheng, M. S. Chen, R. Huang, S. H. Zhang, Z. C. Zhao, J. Mao, X. Y. Meng, Q. Q. Ji, G. J. Hou, X. W. Han, X. H. Bao, Y. Wang, D. H. Deng, *Nat. Catal.* **2021**, *4*, 242.

[46] W. Q. Han, Z. H. Liu, Y. B. Pan, G. N. Guo, J. X. Zou, Y. Xia, Z. M. Peng, W. Li, A. G. Dong, *Adv. Mater.* **2020**, *32*, 2002584.

[47] J. Deng, H. B. Li, S. H. Wang, D. Ding, M. S. Chen, C. Liu, Z. Q. Tian, K. S. Novoselov, C. Ma, D. H. Deng, X. H. Bao, *Nat. Commun.* **2017**, *8*, 14430.

[48] M. K. Liu, P. Zhang, Z. H. Qu, Y. Yan, C. Lai, T. X. Liu, S. Q. Zhang, *Nat. Commun.* **2019**, *10*, 3917.

[49] X. Zhang, H. Wang, G. Wang, *J. Colloid Interface Sci.* **2017**, *492*, 41.

[50] X. Zhang, B. B. Wang, G. Wang, X. J. Liu, H. Wang, *Electrochim. Acta* **2017,** *258*, 764.

[51] X. Zhang, X. J. Liu, G. Wang, H. Wang, *J. Colloid Interface Sci.* **2017**, *505*, 23.

[52] F. H. Yang, H. Gao, H. N. Hao, S. L. Zhang, P. Li, Y. Q. Liu, J. Chen, Z. P. Guo, *Adv. Funct. Mater.* **2019**, 29, 1808291.

[53] X. J. Wang, S. Zhang, Y. Shan, L. Chen, G. Y. Gao, X. L. Zhu, B. Cao, X. M. He, *Energy Storage Materials* **2021**, *37*, 55.

[54] Y. Li, R. P. Zhang, W. Zhou, X. Wu, H. B. Zhang, J. Zhang, *ACS Nano* **2019**, *13*, 5533.

[55] J. J. Wang, C. Luo, T. Gao, A. Langrock, A. C. Mignerey, C. S. Wang, *Small* **2015**, *11*, 473.

Mesoporous single layered MoS$_2$/carbon composite is successfully synthesized and displays remarkable electrochemical performance for both sodium ion batteries and sodium ion full cells. The reaction mechanism has been systematically investigated by *in situ* and *ex situ* characterizations. This work might be expected to guide the future designing protocol for various mesoporous single layered transition metal sulfide/carbon composite materials.

Xing Zhang,Wei Weng, Hao Gu, Zibo Hong, Wei Xiao, Feng (Ryan) Wang, Wei Li, Dong Gu*

A Versatile Preparation of Mesoporous Single Layered Transition Metal Sulfide/Carbon Composites for Enhanced Sodium Storage